WATER RESOURCES RESEARCH, VOL. 49, 1–12, doi:10.1002/2013WR013999, 2013

Hybrid modeling of heterogeneous geochemical reactions in fractured porous media

Delphine Roubinet[1] and Daniel M. Tartakovsky[1]

Received 18 April 2013; revised 8 October 2013; accepted 4 November 2013.

[1] Quantitative modeling of geochemical reactions at the Darcy scale is challenging due to their dependence on pore-scale characteristics that often cannot be averaged out. We propose a hybrid pore-scale/continuum-scale algorithm to bridge the gap between the pore-scale mechanisms of reactive transport and the Darcy-scale observations of their impact. These two scales are coupled by introducing extra nodes at the pore/continuum interfaces, in which the continuity of both concentrations and mass fluxes is enforced. Our algorithm is applicable to highly localized transport phenomena that can be adequately described by Darcy-scale equations in most of a computational domain except for small regions (e.g., reaction fronts) wherein pore-scale simulations are necessary. We employ the proposed hybrid algorithm to model transient reactive solute transport involving fracture cementation.

Citation: Roubinet, D., and D. M. Tartakovsky (2013), Hybrid modeling of heterogeneous geochemical reactions in fractured porous media, *Water Resour. Res.*, *49*, doi:10.1002/2013WR013999.

1. Introduction

[2] Physical, chemical, and biological processes affecting the fate and transport of solutes in natural environments occur and interact on a large range of spatial and temporal scales. Capturing the evolution and interactions of hydraulic and (bio)geochemical properties requires a synthesis of (field and laboratory) experimentation and mathematical modeling. While computational studies elucidated a number of pore-scale transport mechanisms, they can only be used to describe (bio)geochemical phenomena at small scales.

[3] Effective (Darcy-scale or continuum-scale) models of flow and transport are derived by averaging (upscaling) their pore-scale counterparts. These analyses are invaluable in providing fundamental understanding of Darcy-scale models, thus enhancing confidence in the veracity of their predictions. They can also be used to identify flow and transport regimes in which Darcy-scale models are invalid [*Battiato et al*., 2009; *Battiato and Tartakovsky*, 2011; *Boso and Battiato*, 2013]. When the latter occurs, Darcy-scale models fail to capture a number of experimentally observed phenomena, including heterogeneous geochemical reactions [*Noiriel et al*., 2007] and localized mixing-induced precipitation reactions [*Tartakovsky et al*., 2008a].

[4] The breakdown of Darcy-scale flow and transport models occurs in regions of a computational domain wherein pore-scale gradients of state variables (e.g., fluid pressure or solute concentration) become large [*Battiato et al*., 2009; *Battiato and Tartakovsky*, 2011; *Boso and Battiato*, 2013]. In many, if not most, applications of practical significance, such regions are highly localized, i.e., much smaller than the rest of the computational domain. Hybrid algorithms [*Leemput et al*., 2007; *Tartakovsky et al*., 2008b; *Battiato et al*., 2011] take advantage of this fact by using pore-scale simulations in subdomains where their Darcy-scale counterparts break down and solving Darcy-scale equations elsewhere in the computational domain.

[5] By explicitly dealing with the local breakdown of Darcy-scale (or upscaled) models, hybrid algorithms conceptually differ from their multiscale counterparts that assume that a given phenomenon can be adequately described by models on multiple scales, e.g., on the pore scale and the Darcy scale (see *Battiato et al*. [2011] for a detailed discussion and references). For example, multiscale analyses of *Balhoff et al*. [2008], *Mehmani et al*. [2012], and *Tomin and Lunati* [2013] start from the premise that both pore-scale and Darcy-scale equations are valid and explicitly aim to upscale the state variables (e.g., fluid pressure or solute concentration) from the pore-scale to the Darcy scale. Such methodologies are typically not amenable to a theoretical assessment (mathematical proof) of convergence and existence/uniqueness of a solution. The pore-network models of reactive solute transport [*Balhoff et al*., 2008; *Mehmani et al*., 2012] are currently limited to flow regimes with large Péclet numbers wherein diffusion is neglected [*Mehmani et al*., 2012].

[6] Computationally efficient and robust coupling of pore-scale and Darcy-scale models is, arguably, the central issue of hybrid methods. In general, the coupling requires a computationally expensive iterative procedure to ensure the continuity of state variables and their fluxes along the interface separating the domains in which pore-scale and Darcy-scale models are solved [*Leemput et al*., 2007; *Tartakovsky et al*., 2008b]. The need for iterations (i.e., for

[1]Department of Mechanical and Aerospace Engineering, University of California, San Diego, La Jolla, California, USA.

Corresponding author: D. Roubinet, Department of Mechanical and Aerospace Engineering, University of California, San Diego, 9500 Gilman Dr., La Jolla, CA 92093, USA. (delphine.roubinet@gmail.com)

0043-1397/13/10.1002/2013WR013999

multiple solves of the pore-scale and Darcy-scale codes at each time step) can be obviated at the cost of reducing a hybrid algorithm's generality. For example, the hybrid strategy of *Tartakovsky et al*. [2008b] avoids iterations by employing smoothed particle hydrodynamics to solve both pore-scale and Darcy-scale reaction-diffusion equations; incorporation of advection into this hybrid strategy remains a challenge.

[7] A major goal of our analysis is to introduce a hybrid algorithm that preserves a maximal degree of generality (e.g., handles space-time varying flow velocity and pore-geometry alterations due to precipitation and/or dissolution), while replacing numerical iterations at the pore-scale/Darcy-scale interface with a semianalytical coupling. In so doing, we build upon the hybrid algorithm of *Battiato et al*. [2011], in which a modified finite-volume method and an iterative procedure were used to enforce, respectively, the continuity of mass and mass fluxes at the pore-scale/Darcy-scale interface. Like *Battiato et al*. [2011], we use our hybrid algorithm to model highly localized heterogeneous reactions in a fracture. Unlike *Battiato et al*. [2011] who considered steady-state fully developed flow described analytically by Poiseuille's law, we solve Stokes flow equations numerically. This enables us to account for local alterations of the velocity field caused by solute precipitation on fracture walls.

[8] More important from the algorithmic point of view, we replace the computationally demanding iterative coupling of the pore-scale and Darcy-scale solvers [*Battiato et al*., 2011] with a semianalytical coupling technique in which one of the continuity conditions (e.g., mass conservation) is satisfied automatically, while the second one (e.g., continuity of mass fluxes) is formulated as an implicit boundary condition [*Roubinet et al*., 2012]. The finite-volume method is modified by replacing the common analytical interpolators with their numerical counterparts at the pore-scale/continuum-scale interface. The new interpolators are expressed explicitly at both the pore and Darcy scales, and the continuity of mass and mass fluxes is built explicitly into the final numerical scheme (a discretized finite-volume matrix).

[9] The equations used to model flow and reactive transport at the pore and Darcy scales are described in section 2. A general formulation of our hybrid algorithm is provided in section 3. Model validation results are provided in section 4. In section 5, we use our hybrid algorithm to model heterogeneous geochemical reactions and accumulation of precipitated material at the entrance of a fracture.

2. Problem Formulation

[10] We consider both pore-scale and Darcy-scale descriptions of fluid flow and reactive solute transport.

2.1. Pore-Scale Equations

[11] Inside the pore space of a porous medium, single-phase flow of an incompressible fluid with density ρ and dynamic viscosity μ can be described by the Stokes and continuity equations

$$\mu\nabla^2\mathbf{u}+\rho\mathbf{g}-\nabla p=0, \qquad \nabla\cdot\mathbf{u}=0. \tag{1}$$

[12] Here $\mathbf{u}(\mathbf{x},t)$ is the pore-scale flow velocity, $p(\mathbf{x},t)$ is the fluid pressure, and $\mathbf{g}$ is the gravitational acceleration vector. Equation (1) is subject to no-slip and no-flow boundary conditions at fluid-solid interfaces, as well as to boundary conditions imposed on a porous medium's outer surface.

[13] The fluid contains a solute with concentration $c(\mathbf{x},t)$, whose pore-scale dynamics is described by an advection-diffusion equation (ADE)

$$\frac{\partial c}{\partial t}+\nabla\cdot(\mathbf{u}c)=D_m\nabla^2 c, \tag{2}$$

where D_m is the molecular diffusion coefficient. This equation is subject to boundary conditions imposed on the porous medium's outer surface. The solute reacts with solid matrix, with the surface reaction rate $r_s(c)$. Mass concentration at the fluid-solid interfaces takes the form [e.g., *Tartakovsky et al*., 2008b]

$$-\mathbf{n}\cdot(D_m\nabla c)=r_s(c), \tag{3}$$

where $\mathbf{n}$ is the outward normal unit vector to the interfaces. This heterogeneous reaction changes the pore geometry of the solid matrix. Let $v_n(\mathbf{x}_s,t)$ denote the normal component of the velocity with which a point $\mathbf{x}_s$ on the solid surface moves as a result of either solute precipitation or surface dissolution. It is directly proportional to surface reaction rate r_s [e.g., *Tartakovsky et al*., 2008b],

$$v_n(\mathbf{x}_s)=\frac{r_s}{\rho_s}, \tag{4}$$

where ρ_s is the density of the solid phase.

2.2. Darcy-Scale Equations

[14] The pore-scale flow equation (1) is replaced by Darcy's law and Darcy-scale mass conservation,

$$\mathbf{U}=-\mathbf{K}\nabla h, \qquad \frac{\partial\omega}{\partial t}=-\nabla\cdot\mathbf{U}. \tag{5}$$

[15] Here $\mathbf{U}(\mathbf{X},t)$ is the macroscopic flow velocity at a Darcy-scale point $\mathbf{X}=(X_1,X_2,X_3)^\top$ (i.e., a representative elementary volume associated with this continuum-scale representation), $\mathbf{K}(\mathbf{X},t)$ is the hydraulic conductivity of a porous medium (in general, a second-rank tensor), $h(\mathbf{X},t)=\overline{p}/(\rho g)+X_3$ is the Darcy-scale hydraulic head, $\overline{p}(\mathbf{X},t)$ is the Darcy-scale pressure, and $\omega(\mathbf{X},t)$ is the porous medium's porosity.

[16] The Darcy-scale solute concentration $\overline{c}(\mathbf{X},t)$ satisfies an advection-reaction-dispersion equation (ARDE)

$$\frac{\partial\omega\overline{c}}{\partial t}+\nabla\cdot(\mathbf{U}\overline{c})=\nabla\cdot(\mathbf{D}\nabla\overline{c})-R(\overline{c}), \tag{6}$$

where $\mathbf{D}$ is the dispersion coefficient (a second-rank tensor). While the heterogeneous reactions enter the pore-scale description through the boundary condition (3), in the Darcy-scale transport model (6) they are represented by the

homogeneous reaction term $R(\overline{c})$ and time-varying porosity ω. For the moment, we keep the pore-scale heterogeneous reaction rate law $r_s(c)$ and its Darcy-scale homogeneous counterpart $R(\overline{c})$ generic in order to preserve the ability of the hybrid algorithm described below to deal with a wide class of heterogeneous reactions. Concrete examples of these laws are presented in sections 4 and 5.

3. Hybrid Models

[17] The Darcy-scale flow and transport equations can be derived from their pore-scale counterpart by various homogenization (upscaling) techniques. These approaches also establish conditions under which the Darcy-scale flow and transport equations become invalid [*Battiato et al.*, 2009; *Battiato and Tartakovsky*, 2011; *Boso and Battiato*, 2013]. Let Ω denote a simulation domain (a porous medium of interest), and suppose that the Darcy-scale equations break down in a small part of this domain, Ω_p ($\Omega_p \subset \Omega, ||\Omega_p|| \ll ||\Omega||$), wherein the pore-scale equations are to be solved. The Darcy-scale equations are solved in the rest of the computational domain, Ω_c ($\Omega = \Omega_p \cup \Omega_c$).

[18] The pore-scale and Darcy-scale simulations are coupled by enforcing the continuity of mass (concentration) and mass flux (its normal component) along the interface Γ between Ω_p and Ω_c,

$$\overline{c}(\mathbf{X},t) = \frac{1}{||\Gamma_l||}\int_{\Gamma_l} c(\mathbf{x},t)\mathrm{d}\mathbf{x} \tag{7a}$$

$$\overline{q}(\mathbf{X},t) = \frac{1}{||\Gamma_l||}\int_{\Gamma_l} q(\mathbf{x},t)\mathrm{d}\mathbf{x}. \tag{7b}$$

[19] Here Γ_l and Γ_s are the parts of the interface Γ occupied, respectively, by the liquid and the solid, $\Gamma = \Gamma_l \cup \Gamma_s$; and q and $\overline{q}$ are the normal component of pore-scale and Darcy-scale mass fluxes $\mathbf{q} = \mathbf{u}c - D_m\nabla c$ and $\overline{\mathbf{q}} = \mathbf{U}\overline{c} - \mathbf{D}\nabla\overline{c}$, respectively.

3.1. Numerical Discretization

[20] To simplify the presentation, we consider a transport phenomenon that is described by either the one-dimensional Darcy-scale equations or the two-dimensional pore-scale equations. Figure 1 shows a hybrid discretization in which the Darcy-scale domain is discretized into N_V one-dimensional volumes V_I ($I = 1, \ldots, N_V$) (in Figure 1, $N_V = 4$), and the pore-scale domain is discretized with a two-dimensional grid composed of volumes $v_{i,j}$ ($i = 1, \ldots, n_x$ and $j = 1, \ldots, n_y$), where n_x and n_y are the number of volumes in the x and y directions (in Figure 1, $n_x = n_y = 4$).

3.1.1. Finite-Volume Method for Interior Elements

[21] The pore-scale and Darcy-scale unknowns are computed at the center (big red dots and small green dots in Figure 1, respectively) of each discretization volume. Without loss of generality, in the pore-scale domain Ω_p we use a constant time step Δ_t and pore-scale elements $v_{i,j}$ of constant lengths Δ_x and Δ_y in the x and y directions, respectively. Integrating equation (2) over the pore-scale volume $v_{i,j}$ leads to its regular finite-volume representation

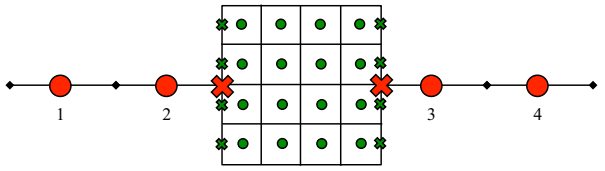

Figure 1. Hybrid finite-volume discretization. The (small green and big red) circles indicate nodes at which the (pore-scale and Darcy-scale) unknowns are computed with a regular finite-volume method. The (big red and small green) crosses denote extra nodes used to enforce the continuity conditions at the hybrid's interfaces.

$$c_{i,j}^{n+1} = c_{i,j}^{n} - \frac{\sigma_{i,j}^{n}(w,e)}{\Delta_x} - \frac{\sigma_{i,j}^{n}(s,n)}{\Delta_y} \tag{8}$$

where $c_{i,j}^n$ is the pore-scale concentration at the center of volume $v_{i,j}$ ($i = 1, \ldots, n_x$ and $j = 1, \ldots, n_y$) at time $t_n = n\Delta_t$; $\sigma_{i,j}^n(\alpha,\beta) = g_n[q_{i,j}(\alpha)] + g_n[q_{i,j}(\beta)]$; $q_{i,j}(k)$ are the spatially discretized versions of mass flux $q(k) = \mathbf{n}_k \cdot (\mathbf{u}c - D_m\nabla c)$ normal to the k ($k = w$, e, s, or n representing the west, east, south, or north) edge of volume $v_{i,j}$; and

$$g_n(z) = \left[\theta z^{n+1} + (1-\theta)z^n\right]\Delta_t. \tag{9}$$

[22] Setting $\theta = 0$, 0.5, or 1 one obtains an explicit, Crank-Nicolson, or implicit method. Mass flux $q(k)$ is discretized as

$$q_{i,j}(k) = a_{i,j}^k c_{i_k,j_k} + \tilde{a}_{i,j}^k c_{i,j}, \tag{10}$$

where c_{i_k,j_k} is the pore-scale concentration at the center of volume v_{i_k,j_k} that shares the edge k of the volume $v_{i,j}$. The hybrid differencing scheme [*Versteeg and Malalasekera*, 2007, section 5.7] is used to compute coefficients $a_{i,j}^k$ and $\tilde{a}_{i,j}^k$. They are obtained by applying a central difference scheme to the diffusive term and either a central difference scheme (for small Péclet numbers) or an upwind scheme (for large Péclet numbers) for the advective term. Only the central difference scheme was tested in the present analysis.

[23] Without loss of generality, in the (one-dimensional) Darcy-scale domain Ω_c we use a constant time step Δ_T and Darcy-scale elements V_I of constant lengths Δ_X in the x direction. Integrating the one-dimensional version of equation (6) over the Darcy-scale volume V_I leads to its regular finite-volume representation

$$\omega_I^{N+1}\overline{c}_I^{N+1} = \omega_I^N\overline{c}_I^N - \frac{g_N[\overline{q}_I(W)] + g_N[\overline{q}_I(E)]}{\Delta X} - g_N[R(\overline{c}_I)] \tag{11}$$

where $\overline{c}_I^N$ is the concentration at the center of volume V_I at time $t_N = N\Delta_T$, and

$$g_N(z) = \left[\theta z^{N+1} + (1-\theta)z^N\right]\Delta_T. \tag{12}$$

[24] The spatially discretized versions of mass flux $\overline{q}(K) = \mathbf{n}_K \cdot (\mathbf{U}\overline{c} - \mathbf{D}\nabla\overline{c})$ normal to the K ($K = W$ and E, representing the west and east) edge of volume V_I are given by

$$\overline{q}_I(K)=A_I^K\overline{c}_{I_K}+\tilde{A}_I^K\overline{c}_I, \tag{13}$$

where $\overline{c}_{I_K}$ is the Darcy-scale concentration at the center of volume V_{I_K} that shares the edge K of the volume V_I, and coefficients A_I^K and $\tilde{A}_I^K$ are defined by the numerical procedure used to compute their counterparts in equation (10).

3.1.2. Finite-Volume Method for Interfacial Elements

[25] Along the pore-scale/Darcy-scale interface Γ, where the pore-scale and Darcy-scale volumes are adjacent to each other (e.g., at the nodes denoted by the big red and small green crosses in Figure 1), interior finite-volume representations (8) and (11) are modified as follows. Let I-K denote the edges ($K = W$ or E) of the Darcy-scale volumes V_I adjacent to the interface Γ (the big red crosses 2-E and 3-W in Figure 1). Let (i,j)-k denote the edges ($k = w$, e, s, or n) of the pore-scale volumes $v_{i,j}$ adjacent to the interface Γ (the small green crosses $(1,j)$-w and (nx,j)-e, with $j=1,\ldots,n_y$, in Figure 1). Finally, let $\overline{c}_{I\text{-}K}$ denote the Darcy-scale concentrations at the I-K edges and $c_{(i,j)\text{-}k}$ denote pore-scale concentrations at the (i,j)-k edges.

[26] We treat extra unknowns $\overline{c}_{I\text{-}K}$ and $c_{(i,j)\text{-}k}$ as Dirichlet boundary conditions for the corresponding interfacial control volumes. The corresponding mass fluxes at the edges forming Γ are obtained by modifying equations (10) and (13),

$$q_{i,j}(k)=b_{i,j}^k c_{(i,j)\text{-}k}+\tilde{b}_{i,j}^k c_{i,j} \tag{14}$$

and

$$\overline{q}_I(K)=B_I^K\overline{c}_{I\text{-}K}+\tilde{B}_I^K\overline{c}_I \tag{15}$$

for all i, j, I, k, and K that belong to the pore-scale/Darcy-scale interface Γ. Coefficients $b_{i,j}^k$ and $\tilde{b}_{i,j}^k$ are obtained from coefficients $a_{i,j}^k$ and $\tilde{a}_{i,j}^k$ by enforcing Dirichlet boundary condition on the edge k of the volume $v_{i,j}$, and coefficients B_I^K and $\tilde{B}_I^K$ are obtained from coefficients A_I^K and $\tilde{A}_I^K$ by enforcing Dirichlet boundary condition on the edge K of the volume V_I.

3.1.3. Global Linear System

[27] Continuity conditions (7) are spatially discretized as

$$\overline{c}_{I\text{-}K}=\frac{\Delta_y}{H_I^K}\sum_{j=1}^{n_y}c_{(i',j)\text{-}k}\quad \overline{q}_I(K)=-\frac{\Delta_y}{H_I^K}\sum_{j=1}^{n_y}q_{i',j}(k) \tag{16}$$

where $i'=1$ (or n_x) for the west (or east) edge of the two-dimensional pore-scale simulation domain, whose widths at the (west, $K = W$, or east, $K = E$) pore-scale/Darcy-scale interfaces are H_I^W and H_I^E. We replace equation (16) with

$$c_{(i',j)\text{-}k}=\alpha_{i',j}\overline{c}_{I\text{-}K}\qquad q_{i',j}(k)=-\beta_{i',j}\overline{q}_I(K) \tag{17}$$

where the (unknown) coefficients $\alpha_{i',j}$ and $\beta_{i',j}$ satisfy

$$\frac{\Delta_y}{H_I^K}\sum_{j=1}^{n_y}\alpha_{i',j}=1\qquad \frac{\Delta_y}{H_I^K}\sum_{j=1}^{n_y}\beta_{i',j}=1. \tag{18}$$

[28] A global linear system for our hybrid finite-volume method is composed of (i) concentrations computed with equations (8) and (11) for interior pore-scale and Darcy-scale control volumes, respectively; (ii) concentrations computed with equations (8) and (14) for interfacial pore-scale control volumes; (iii) concentrations computed with equations (11) and (15) for interfacial Darcy-scale control volumes, and (iv) the continuity conditions at the pore-scale/Darcy-scale interface Γ (Appendix A). The latter can be implemented in one of the two alternative ways. The first, which we refer to as "free concentration coupling" or FCC, combines the first equation in (16) and the second equation in (17). The second, denoted by the term "free mass flux coupling" or FFC, combines the second equation in (16) and the first equation in (17). Solution of the resulting system of linear algebraic equations yields both concentrations at the centers of pore-scale and Darcy-scale control volumes and concentrations at the pore-scale/Darcy-scale interface.

[29] FCC and FFC do not require prior knowledge of the relationship between the pore-scale and Darcy-scale concentration and mass flux, respectively. Instead, FCC and FFC assume coefficients $\beta_{i',j}$ and $\alpha_{i',j}$, respectively. The choice between FCC and FFC depends on whether the pore-scale concentration or the pore-scale flux can be treated as piecewise constant (over the edge of an adjacent Darcy-scale control volume) at the pore-scale/Darcy-scale interfaces. For example, if pore-scale transport is diffusion-dominated then the pore-scale concentration at the pore-scale/Darcy-scale interface (i.e., in the region of validity of the Darcy-scale description) is approximately constant over the bounding edge of the adjacent Darcy-scale control volume. Then, one can use FFC with $\alpha_{i',j}=1$ for all i' and j belonging to the interface Γ (in our example, $i'=1, n_x$ and $1 \le j \le n_y$). Sections 4 and 5.1 illustrate configurations where the assumption $\beta_{i',j}=1$ with FCC and $\alpha_{i',j}=1$ with FFC hold, respectively.

[30] Regardless of whether FCC or FFC is used, our hybrid algorithm results in a global linear system (Appendix A)

$$\mathbf{Ac}=\mathbf{b} \tag{19}$$

where $\mathbf{A}$ is an $N_c \times N_c$ matrix, $\mathbf{c}$ and $\mathbf{b}$ are vectors of length N_c, and N_c is the total number of unknowns (concentrations assembled into vector $\mathbf{c}$)

$$N_c=N_V+2N_{I^*}+\sum_{I^*=1}^{N_{I^*}}f(I^*). \tag{20}$$

[31] Here N_{I^*} is the number of hybrid nodes; $f(I^*)=n_x(I^*)n_y(I^*)+2n_y(I^*)$ defines the number of pore-scale unknowns in hybrid node I^*; and $n_x(I^*)$ and $n_y(I^*)$ are the numbers of pore-scale control volumes discretizing the hybrid node I^* in the x and y directions, respectively.

3.2. Numerical Implementation

3.2.1. Flow Computation and Coupling

[32] Pore-scale flow equations (1) are solved by using a finite-difference method on a fully staggered grid [*Gerya*, 2010]. At the pore-scale/Darcy-scale interfaces, the Darcy-scale flow variables (pressure and/or flow velocity) are used as boundary conditions for the pore-scale simulations. It is worthwhile emphasizing that this study focuses on transport

phenomena whose Darcy-scale descriptions break down locally due to, e.g., high concentration gradients caused by biochemical heterogeneity. In such a setting, Darcy-scale flow equations remain valid throughout a computational domain, even in regions where their transport counterparts are not.

3.2.2. Time-Scale Coupling

[33] Solute concentrations are determined by solving the global linear system (19) at each Darcy-scale time step Δ_T. If the pore-scale subdomains require a smaller time step ($\Delta_t < \Delta_T$), then pore-scale concentrations between two Darcy-scale times t_N and t_{N+1} are determined at each pore-scale time $t_n = n\Delta_t$ where $n = 1, \ldots, n_t - 1$ with $n_t\Delta_t = \Delta_T$. Initial conditions for these pore-scale simulations are given by the concentrations computed at time t_N and boundary conditions are provided by equations (17) at time t_N (the first or second of these equations for FFC or FCC, respectively). Continuity conditions are updated by solving the global linear system (19) when reaching the Darcy-scale time t_{N+1}, corresponding to $t_n = n_t\Delta_t$.

3.2.3. Algorithm Acceleration

[34] Changes in pore-geometry due to biochemical deposition/dissolution processes usually occur at a time scale that is much (several orders of magnitude) larger than typical time scales Δ_t and Δ_T. This allows one to significantly increase the hybrid algorithm's efficiency by treating the concentration as time-invariant during each time step, Δ_t^g, of surface growth [*Dijk and Berkowitz*, 1998].

[35] In the absence of surface growth (early stages of surface chemistry simulations), the global linear system (19) is solved at each time step Δ_T; in later stages of our hybrid simulations (19) is solved at each time step Δ_t^g. We use the sparse solver from `umfpack` library [*Davis*, 2004], where matrix and vector storage is optimized by using `uBLAS` library from project Boost, `http://www.boost.org`.

3.2.4. Pore-Geometry Evolution

[36] At the Darcy scale, the system parameters affected by these processes are porosity ω, Darcy flow velocity $\mathbf{U}$, dispersion coefficient $\mathbf{D}$, and the reaction term $R(\overline{c})$. Since our hybrid algorithm models highly localized reaction fronts with pore-scale simulations (in Ω_p), the temporal variability of these Darcy-scale parameters in the rest of a computational domain (Ω_c) can often be neglected. Alternatively, one can incorporate this temporal variability by relying on rigorous homogenization results that relate pore-scale characteristics of a porous medium to its macroscopic properties. In the computational examples below we adopt the latter approach.

[37] At the pore scale, evolution of the solid matrix composed of points $\mathbf{x}_s(t)$ is governed by equation (4). The changing pore space implies that the number of control volumes in the pore-scale domain, n_x and n_y, varies with time. Consequently, the size of the global linear system (19) changes with time. The number of unknowns N_c^n at time $t_n^g = n\Delta_t^g$ is obtained by modifying equation (20),

$$N_c^n = N_V + 2N_{I^*} + \sum_{I^*=1}^{N_{I^*}} f^n(I^*), \tag{21}$$

where $f^n(I^*) = f(I^*) - [n_s^n(I^*) + 2n_{s_i}^n(I^*)]$ is the number of pore-scale unknowns in hybrid node I^* at time $t_n^g = n\Delta_t^g$, and $n_s^n(I^*)$ and $n_{s_i}^n(I^*)$ are the number of inner and interfacial pore-scale elements representing the solid matrix in hybrid node I^* at time $t_n^g = n\Delta_t^g$, respectively. We use a cellular automaton algorithm (Appendix B) to determine active control volumes of the pore-scale domain Ω_p at each time step Δ_t^g.

4. Hybrid Model Verification

[38] As a test bed for our hybrid models, we use a much studied problem of reactive solute transport in a single fracture whose walls are located at $y = -H/2$ and $y = H/2$. The flow is driven by an externally imposed hydraulic head gradient that is aligned with the x coordinate. The fluid carries a solute, which undergoes a first-order heterogeneous reaction with the fracture walls. The surface reaction rate $r_s(c)$ in equation (3) takes the form

$$r_s = k(c - c_{\mathrm{eq}}), \tag{22}$$

where k is the surface reaction rate constant and c_{eq} is the solute concentration in equilibrium with the solid. This reaction rate law was used to model precipitation/dissolution processes [*Tartakovsky et al*., 2007], sorption reactions [*Berkowitz and Zhou*, 1996], and microbial degradation [*Battiato et al*., 2011]; the latter two studies used $c_{\mathrm{eq}} = 0$.

4.1. Transport Without Surface Growth

[39] At early stages of the process, the surface reaction (22) does not result in surface growth and the fracture wall remains smooth. Away from the fracture edges, flow is fully developed, i.e., pore-scale velocity $\mathbf{u} = (u(y), 0, 0)^\top$ is given by the Poiseuille solution of flow equations (1),

$$\frac{u(y)}{u_m} = 1 - \frac{4y^2}{H^2}, \tag{23}$$

where u_m is the maximum velocity that occurs at the center of the fracture ($y = 0$).

[40] For this problem, the one-dimensional Darcy-scale ARDE (6) is obtained by averaging the pore-scale ADE (2) over y. Using this procedure, *Dijk and Berkowitz* [1998] derived expressions for the Darcy-scale coefficients

$$\frac{D}{D_m} = 1 + \frac{8Pe^2}{945} - \frac{8DaPe^2}{1350(3+Da)}, \tag{24a}$$

$$\frac{U}{u_m} = \frac{2}{3} + \frac{4Da}{15(3+Da)}, \quad R = \frac{D_m}{H^2}\frac{12Da}{3+Da}(\overline{c} - c_{\mathrm{eq}}) \tag{24b}$$

where the Péclet (Pe) and Damköhler (Da) numbers are defined as

$$Pe = \frac{u_m H}{2D_m}, \qquad Da = \frac{kH}{2D_m}. \tag{25}$$

[41] Darcy-scale concentration $\overline{c}(x,t)$ is the transverse average of its pore-scale counterpart,

$$\overline{c}(x_d, t_d) = \frac{1}{H}\int_{-H/2}^{H/2} c(x_d, y, t_d)\mathrm{d}y, \tag{26}$$

where $t_d = 4tD_m/H^2$, $x_d = x/L$, and L is a characteristic length in the longitudinal direction. A solution of the

Darcy-scale ARDE (6) with equation (23) and $c_{eq}=0$ is [*Berkowitz and Zhou*, 1996]

$$\bar{c}=\frac{c_0}{2}\exp\left(\frac{K_1\beta x_d}{2K_2}\right)e^{-\gamma\beta x_d}\mathrm{erfc}\left(\frac{\beta x_d-2K_2\gamma t_d}{2\sqrt{K_2 t_d}}\right)+\frac{c_0}{2}\exp\left(\frac{K_1\beta x_d}{2K_2}\right)e^{\gamma\beta x_d}\mathrm{erfc}\left(\frac{\beta x_d+2K_2\gamma t_d}{2\sqrt{K_2 t_d}}\right) \quad (27)$$

where $\beta=2L/(HPe)$, $\gamma=\sqrt{K_1^2+4K_0K_2}/(2K_2)$, $K_0=3Da/(3+Da)$, $K_1=U/u_m$, and $K_2=D/(D_mPe^2)$.

[42] We use the analytical solution (27) to verify our hybrid algorithm. Unless otherwise specified, the simulations reported below correspond to $H=2\times10^{-4}$ m, $D_m=10^{-9}$ m^2/s, and $u_m=10^{-5}$ m/s, i.e., to $Pe=1$. Following the problem formulation in *Berkowitz and Zhou* [1996], we choose pore-scale boundary conditions $c(x_d=0,y,t_d)=c_0$ and $c(x_d=1,y,t_d)=0$ and the initial condition $c(x_d,y,t_d=0)=0$. The corresponding Darcy-scale conditions are obtained from equation (26). The hybrid simulations are conducted with $\Delta_X=10^{-5}$ m and $\Delta_x=\Delta_y=10^{-6}$ m.

[43] Figure 2 exhibits temporal snapshots of the relative Darcy-scale concentration $\bar{c}(x_d,t_d)/c_0$ computed with the analytical solution (27) (lines with crosses) and hybrid simulations (lines with squares) for $k=10^{-5}$ (full lines) and 10^{-3} m/s (dashed lines). (Time stepping $\Delta_{T_d}=\Delta_{t_d}=10^{-1}$ and 1 was used for the simulations reported in Figures 2a and 2b, respectively.) The agreement between the two solutions demonstrates the accuracy of our hybrid algorithm.

4.2. Transport With Uniform Surface Growth

[44] As time progresses, the surface reaction (22) causes the wall geometry to change due to either solute precipitation on the walls or the wall dissolution. Consequently, the fracture's aperture varies in space and time, $H=H(x,t)$. Since the fracture walls consist of points $\mathbf{x}_s=(x,\pm H/2)^\top$, the solid surface growth equation (4) takes the form

$$\frac{dH}{dt}=-\frac{2k}{\rho_s}[c(x,H/2,t)-c_{eq}],\qquad H(x,0)=H_0. \quad (28)$$

[45] For the purpose of algorithm verification, we consider a transport regime in which the pore-scale solute concentration at the walls remains constant during the simulation time, $c(x,H/2,t)\equiv c_0$. (This somewhat artificial setting is dispensed with in the following section.) Then, equation (28) predicts a linear decrease of the fracture aperture with time (for small enough t),

$$H(t)=H_0-\frac{2k}{\rho_s}(c_0-c_{eq})t. \quad (29)$$

[46] This temporal variability of the pore-scale simulation domain is handled by the cellular automaton algorithm. The temporal variability of the fracture aperture (29) affects the Darcy-scale one-dimensional ARDE (6) by rendering the macroscopic coefficients (24) time dependent.

[47] Figure 3 shows the relative Darcy-scale concentration $\bar{c}/c_0$ computed with the Darcy-scale one-dimensional ARDE (6) (lines with crosses) and hybrid simulations (lines with squares) for (a) $k=10^{-5}$ m/s at times $t_d=2\times10^3$ (full lines) and 8×10^3 (dashed lines) and (b) $k=10^{-3}$ m/s at times $t_d=2\times10^1$ (full lines) and 8×10^1 (dashed lines). The solid phase density ρ_s is set to 10^4 g/m^3. The agreement between the two solutions demonstrates the accuracy of our hybrid algorithm.

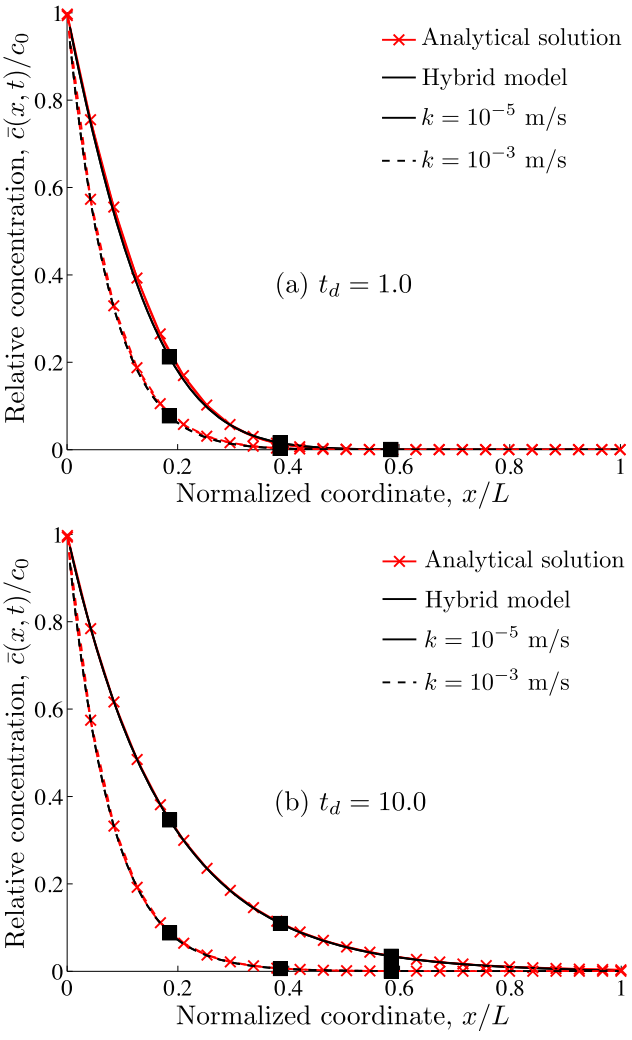

Figure 2. Relative Darcy-scale concentration, $\bar{c}/c_0$, computed with the analytical solution (27) (lines with crosses) and hybrid simulations (lines with squares) for reaction rate $k=10^{-5}$ (solid lines) and 10^{-3} m/s (dashed lines) at dimensionless times (a) $t_d=1$ and (b) $t_d=10$. Squares represent pore-scale simulation domains.

5. Application to Fracture Clogging

[48] The test cases used above dealt with idealized situations in which the Darcy-scale flow and transport equations were valid at every point of a simulation domain. Even in such cases, the complex interplay between changes in pore-geometry induced by heterogeneous (bio)chemical reactions and macroscopic transport characteristics manifests itself in the presence of phenomenological constitutive laws (e.g., relationships between hydraulic conductivity and porosity or between porosity and solute concentration) in Darcy-scale equations of reactive transport. Moreover, the applicability of Darcy-scale transport models is not

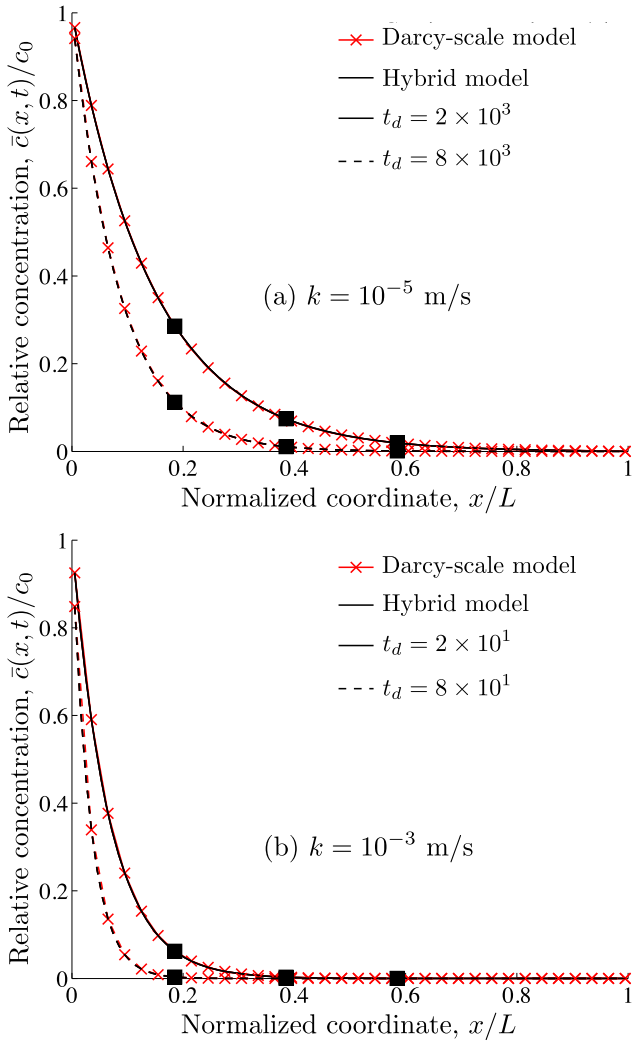

Figure 3. Relative Darcy-scale concentration, $\overline{c}/c_0$, computed with the Darcy-scale ARDE (6) (lines with crosses) and the hybrid algorithm (lines with squares), for (a) $k=10^{-5}$ m/s at times $t_d=2\times10^3$ and 8×10^3 and for (b) $k=10^{-3}$ m/s at times $t_d=2\times10^1$ and 8×10^1.

universal; instead, it is limited to certain flow and transport regimes that can be characterized by their Péclet (*Pe*) and Damköhler (*Da*) numbers [*Battiato et al*., 2009; *Battiato and Tartakovsky*, 2011; *Boso and Battiato*, 2013].

[49] Fracture clogging due to solute precipitation on fracture walls provides an ideal setting to study such a breakdown. *Mikelic et al*. [2006] used upscaling (averaging) of pore-scale flow and transport equations (1)–(4) to model Taylor-Aris hydrodynamic dispersion, which is described by the one-dimensional version of ARDE (6) with $\omega = 1$ and the transport parameters

$$\frac{D}{D_m} = 1 + \frac{8Pe^2}{945}, \qquad \frac{U}{u_m} = \frac{2}{3} + \frac{4Da}{45}, \tag{30a}$$

$$R = \frac{2k}{H}\left(1 - \frac{Da}{3}\right)\overline{c}. \tag{30b}$$

[50] Note that these expressions are qualitatively similar but not identical to formulae (24) derived by *Dijk and Berkowitz* [1998]. *Battiato and Tartakovsky* [2011] identified a specific range of validity of this ARDE in terms of the phase diagram in the space of *Pe* and *Da*. We use our hybrid algorithm to model fracture clogging under conditions of *local* breakdown of ARDE (6).

[51] Unless otherwise specified, the simulation results presented in this section correspond to fracture width $H=10^{-4}$ m, fracture length $L=10^{-3}$ m, maximum (centerline) flow velocity $u_m=10^{-5}$ m/s, molecular diffusion coefficient $D_m=10^{-9}$m^2/s, and equilibrium concentration $c_{\text{eq}}=0.0$ g/m^3. The auxiliary conditions are $c(0,y,t)=c_0=1.0$ g/m^3, $c(L,y,t)=0.0$ g/m^3, and $c(x,y,0)=0.0$ g/m^3. Note that this choice of parameters results in $Pe=0.5$; several values of *Da* are considered below.

[52] In the present section, the Darcy-scale domain Ω_c is discretized with $\Delta_X=10^{-4}$ m (length of continuum-scale elements). Other discretization parameters are indicated for each simulation. The hybrid implementation relies on FFC with all β's in (17) set to 1. In the absence of heterogeneous reactions (section 5.1), flow velocity $u(y)$ is described by Poiseuille's law (23). To account for local surface growth due to solute precipitation (section 5.2), we solve the flow equations (1) in the pore-scale simulation domains Ω_p.

5.1. Surface Chemistry at Fracture Inlet

[53] When reactive solute (with concentration $c = c_0$) enters a fracture that is in equilibrium with a host fluid ($c = c_{\text{eq}}$), the largest concentration gradients and, in accordance with equation (22), the most appreciable solute deposition on fracture walls occur at the fracture inlet. This can lead to a significant reduction in hydraulic conductivity of the fracture, even if overall porosity remains nearly unchanged. Capturing this highly localized phenomenon with a Darcy-scale model would require an artificial rigging of the macroscopic parameters, while using a pore-scale model throughout the whole fracture is not computationally feasible. This situation calls for the deployment of a hybrid model that combines pore-scale simulations in the vicinity of a fracture's inlet with a Darcy-scale model elsewhere. In the simulations reported in this section, the pore-scale domain is $0 \le x \le L/5$ and the Darcy-scale domain is $L/5 \le x \le L$.

[54] Figure 4 provides temporal snapshots (at $t = 10$ s) of relative Darcy-scale concentration, $\overline{c}(x,t)/c_0$, plotted as a function of the relative distance from the fracture inlet, $x_d=x/L$. The concentration $\overline{c}(x,t)$ was computed with the pore-scale ADE (2) (solid red lines), the Darcy-scale ARDE (6) (dashed blue lines), and the hybrid algorithm (lines with squares). The discretization parameters are set to $\Delta_x=\Delta_y=10^{-5}$ m and $\Delta_t = 1$ s. Slow reaction rate constants ($k=10^{-6}$ m/s, i.e., $Da = 0.05$, in Figure 4a) fall within the theoretical range of validity of the Darcy-scale ARDE (6) [*Battiato and Tartakovsky*, 2011]. In this regime, both the pore-scale and Darcy-scale models accurately predict the Darcy-scale concentration (see Figure 4a); although not shown here, the same level of agreement was observed for $k=10^{-5}$ m/s or, equivalently, $Da = 0.5$. Faster reaction rates correspond to larger values of *Da*, leading to the breakdown of Darcy-scale descriptions based on ARDEs. Figure 4b confirms this theoretical prediction by demonstrating the inability of the Darcy-scale ARDE

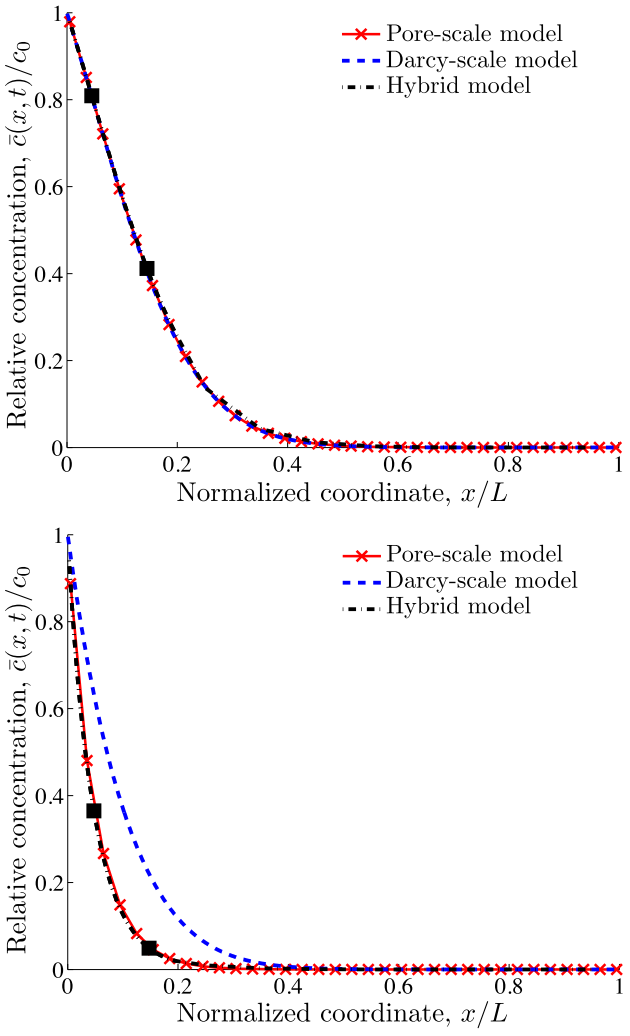

Figure 4. Relative Darcy-scale concentration, $\overline{c}/c_0$, computed with the pore-scale ADE (2) (solid red lines), the Darcy-scale ARDE (6) (dashed blue lines), and the hybrid algorithm (lines with squares), at time $t=10$s for (a) $k=10^{-6}$ m/s and (b) $k=5\times10^{-5}$ m/s. The pore-scale simulation domain is $0 \leq x_d \leq 0.2$.

(6) to correctly predict Darcy-scale concentration (i.e., to predict the pore-scale simulation results, which are treated as exact) for reaction rate $k=5\times10^{-5}$ m/s ($Da=2.5$). Even

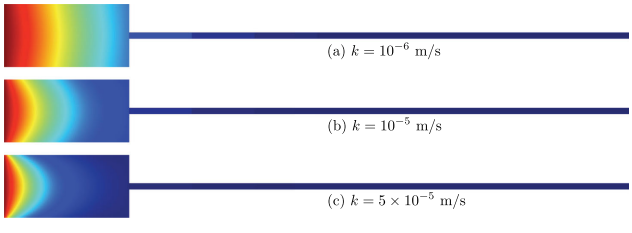

Figure 5. Relative concentration, $c(x,y,t=10\text{s})/c_0$, computed with the hybrid model for (a) $k=10^{-6}$ m/s, (b) $k=10^{-5}$ m/s, and (c) $k=5\times10^{-5}$ m/s. The two-dimensional pore-scale description at the fracture's inlet is coupled with the one-dimensional Darcy-scale representation in the rest of the domain. Relative concentration ranges from 1 (dark red at $x=0$) to 0 (dark blue at $x=L$).

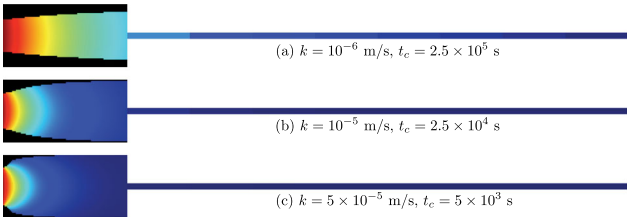

Figure 6. Solute deposition on the fracture's walls (solid black) at the characteristic times t_c corresponding to reaction rate constants (a) $k=10^{-6}$ m/s, (b) $k=10^{-5}$ m/s, and (c) $k=5\times10^{-5}$ m/s. Also shown are respective relative concentration, $c(x,y,t_c)/c_0$ that range from 1 (dark red at $x=0$) to 0 (dark blue at $x=L$). Both are computed with the hybrid algorithm that combine two-dimensional pore-scale simulations in the vicinity of the fracture's inlet with the one-dimensional Darcy-scale simulations elsewhere in the fracture.

in this transport regime, the hybrid algorithm accurately captures the Darcy-scale solute concentration profile predicted with the pore-scale simulations. It does so at the fraction of the computational cost of the latter, reducing the number of unknowns in the global linear system by almost an order of magnitude. The numbers of unknowns used in the hybrid model to capture the Darcy-scale behavior (Figure 4a) and the pore-scale variability (Figure 5) are 131 and 2611, respectively, whereas the pore-scale model requires 1000 and 25000 unknowns to obtain the same results.

[55] By their very nature, the hybrid models provide more information than is contained in the Darcy-scale descriptions. By way of example, Figure 5 exhibits pore-scale variability of the relative solute concentration, $c(x,y,t)/c_0$, in the pore-scale region of the hybrid model, at time $t=10$s for $k=10^{-6}, 10^{-5}$, and 5×10^{-5} m/s. (In these simulations, we set the discretization parameters to $\Delta_x=\Delta_y=2\times10^{-6}$ m and $\Delta_t=1$ s.) As reaction rate constant k increases, transverse variability of the concentration $c(\cdot,y,\cdot)$ becomes more pronounced, invalidating a key assumption that underpins the Taylor-Aris theory of (Darcy-scale) hydrodynamic dispersion. At the same time, faster reaction rates result in sharper reaction fronts, i.e., in a narrower transition zone in which $c(x,\cdot,\cdot)$ decays from 1 to 0. This suggests that the domain of computationally expensive pore-scale simulations, Ω_p, decreases in size as reaction rate constant k increases.

[56] As time increases, the heterogeneous reaction leads to solute deposition on the fracture's wall and to decrease in the fracture's aperture $H(t)$. We define a characteristic time t_c for the fracture to close halfway as a solution of equation $H(t)=H_{0/2}$, where $H(t)$ is given by equation (29). For the parameter values considered in this study, this yields $t_c=2.5\times10^5$s if $k=10^{-6}$ m/s, $t_c=2.5\times10^4$s if 10^{-5} m/s, and $t_c=5\times10^3$s if 5×10^{-5} m/s. Figure 6 shows the fracture walls (solid black) in the end of time period t_c for each of the three values of reaction rate constant k. The discretization parameters are $\Delta_x=\Delta_y=2\times10^{-6}$ m and $\Delta_t^g=10^3$s for $k=10^{-6}$ and 10^{-5} m/s, and 10^2 s for $k=5\times10^{-5}$ m/s. Also shown in this figure are the corresponding solute concentrations that range from 1 (dark red at the fracture's inlet, $x=0$) to 0 (dark blue at the fracture's

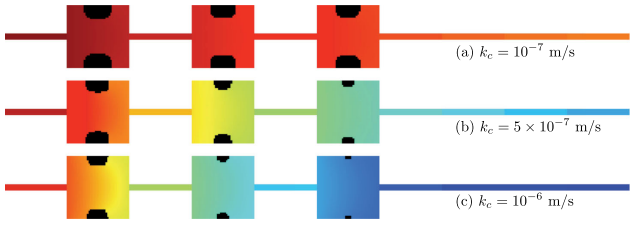

Figure 7. Solute deposition on the fracture's walls (solid black) at time $t=6\times10^4$s in three hot spots ($x=1.5\times10^{-4}, 3.5\times10^{-4}$, and 5.5×10^{-4} m) with high reaction rate constant ($k_h=5\times10^{-5}$ m/s); background reaction rate constants are (a) $k_c=10^{-7}$ m/s, (b) $k_c=5\times10^{-7}$ m/s, and (c) $k_c=10^{-6}$ m/s. Also shown are respective relative concentration, $c(x,y,t_c)/c_0$ that range from 1 (dark red at $x=0$) to 0 (dark blue at $x=L$). Both are computed with the hybrid algorithm that combines two-dimensional pore-scale simulations in the vicinity of the hot spots with the one-dimensional Darcy-scale simulations elsewhere in the fracture.

outlet, $x=L$). As the value of reaction rate constant k increases, the width of the fracture's region with appreciable surface growth decreases and the fracture closes faster.

5.2. Heterogeneous Reaction Rate Constant

[57] Heterogeneous reaction rate constants, which give rise to highly localized surface growth, provide another setting where Darcy-scale models break down and must be replaced with pore-scale or hybrid simulations. We consider a piecewise constant reaction rate constant,

$$k(x)=\begin{cases} k_c & x\in\Omega_c \\ k_h & x\in\Omega_p \end{cases}, \tag{31}$$

where k_c corresponds to Damköhler numbers Da for which the Darcy-scale ADE (6) is valid, and k_h to Da values for which the Darcy-scale ADE (6) breaks down. We set $k_h=5\times10^{-5}$ m/s ($Da=2.5$) at $x=1.5\times10^{-4}, 3.5\times10^{-4}$ and 5.5×10^{-4} m; and $k_c=10^{-7}$ m/s ($Da=0.005$), 5×10^{-7} m/s ($Da=0.025$), or 10^{-6} m/s ($Da=0.05$) in the rest of the simulation domain. The initial concentration is $c(x,y,0)=1.0$ g/m^3, and boundary conditions are $c(0,y,t)=c_0=1.0$ g/m^3 and $\partial c/\partial x=0$ at $x=L$. The discretization parameters are set to $\Delta_x=\Delta_y=2.5\times10^{-6}$ m and $\Delta_t^g=10^2$s.

[58] Figure 7 shows the localized fracture wall growth and corresponding solute concentrations at time $t=6\times10^4$s. While none of the considered values of k_c is sufficient to induce widespread surface growth, they contribute to surface growth in the neighborhoods of hot spots with $k=k_h$ by increasing the spatial variability of solute concentration in the fracture. When $k_c=10^{-7}$ m/s (Figure 7a), solute concentration is close to its initial value in most of the fracture, and the localized fracture wall growth is similar in all three hot spots. Increased background reaction rate constant (e.g., $k_c=10^{-6}$ m/s in Figure 7c) increases the longitudinal variability of solute concentration and facilitates the differentiation in the intensity of surface growth at hot spots.

6. Discussion and Conclusions

[59] We presented a new hybrid approach to model reactive transport in fractured and porous media. It is capable of handling transport processes, which cannot be described with Darcy-scale models and occur in domains that are too large to be covered with pore-scale simulations. Starting from the premise that the failure of Darcy-scale models is confined to small regions of a computational domain, hybrid models combine pore-scale and continuum-scale descriptions. They use pore-scale simulations in such regions and Darcy-scale simulations elsewhere. In our hybrid implementation continuity of concentration and mass flux at the pore-scale/Darcy-scale interfaces is enforced by a modified finite-volume method, which explicitly integrates the continuity conditions into the global linear system.

[60] Hybrid models are particularly useful for quantitative analyses of highly localized phenomena involved in solute precipitation onto the solid matrix and solid matrix dissolution by fluid flowing through a porous material. Such a localization can be induced either by high solute concentration gradients at locations of solvent injection or by spatial heterogeneity of surface reaction rate constants. It occurs, for example, in geotechnical engineering where cementation and clogging phenomena are used to modify or restore soil properties [*Ivanov and Chu*, 2008]. Other application areas vary from remediation of soils modified by human activities to safety enhancement of subsurface storage of toxic chemicals.

[61] Hybrid models provide a means of studying geometric pore-scale variability and/or effects of surface roughness on macroscopic behavior of fluids and solutes in porous media. This can be done by combining the pore-scale component of a hybrid with stochastic representations of pore geometry and roughness. The latter enables one to derive effective characteristics of flow and transport in terms of the statistics of solid surfaces (e.g., mean and standard deviation of fracture aperture) [*Tartakovsky and Xiu*, 2006; *Park et al*., 2012; *Zayernouri et al*., 2013].

[62] Hybrid models can also be incorporated into discrete fracture-network descriptions of transport in fractured rocks. Analyses of highly heterogeneous fracture networks require an efficient representation of their organization, which can be based on simplified models of flow and solute redistribution at intersections of different fractures [*Roubinet et al*., 2010a]. Hybrid models that combine a simple (e.g., one-dimensional Darcy-scale) representation of each fracture and a pore-scale description of processes at their intersections would facilitate such analyses.

[63] While the present analysis employed a finite-volume discretization, our hybrid modeling framework can easily incorporate other numerical methods. For example, the particle-tracking method of *Roubinet et al*. [2010b] can be used to describe particle displacements in both pore-scale and Darcy-scale transport models; a coupling method would determine the pore-scale distribution of particles at the pore-scale/Darcy-scale interfaces.

[64] In the follow-up studies, we will apply our hybrid algorithm to model two-dimensional Darcy-scale transport in porous media with realistic pore geometry. Doing so would require one to express the pore-scale and

Darcy-scale coupling on all the edges of a hybrid node and to consider configurations where several Darcy-scale hybrid nodes are present on each interface and related to a given number of pore-scale nodes.

Appendix A: Global Linear System

[65] When concentration $c(x,y,t)$ is evaluated in all the pore-scale elements discretizing the hybrid node I^*, $f(I^*)$ in equation (20) is expressed as $f(I^*)=n_x(I^*)$ $n_y(I^*)+2n_y(I^*)$, where $n_x(I^*)$ and $n_y(I^*)$ are the number of pore-scale control volumes discretizing the hybrid node I^* in the x and y directions, respectively. Let $l_{i,j}$ denote the index of component $c(l_{i,j})$ of vector **c** that represents pore-scale concentration $c_{i,j}^{n+1}$ at the center of pore-scale volume $v_{i,j}$ at time $t_{n+1}=(n+1)\Delta_t$. Let $l_{i,j}^k$ denote the index of component $c(l_{i,j}^k)$ of vector **c** that represents pore-scale concentration c_{i_k,j_k}^{n+1} at the center of volume v_{i_k,j_k}, which shares the edge k ($k=w$, e, s, or n) with volume $v_{i,j}$.

[66] Finite-volume discretization (8) with pore-scale volumes $v_{i,j}$ contributes the following components to the global finite-volume matrix **A** in equation (19)

$$A(l_{i,j},l_{i,j})=\Delta_x\Delta_y+\theta\Delta_t\Delta_y(\tilde{a}_{i,j}^w+\tilde{a}_{i,j}^e)+\theta\Delta_t\Delta_x(\tilde{a}_{i,j}^s+\tilde{a}_{i,j}^n) \tag{A1}$$

and

$$A(l_{i,j},l_{i,j}^k)=-\theta\Delta_t\Delta_y a_{i,j}^k, \qquad k=w,e \tag{A2}$$

$$A(l_{i,j},l_{i,j}^k)=-\theta\Delta_t\Delta_x a_{i,j}^k, \qquad k=s,n \tag{A3}$$

where $\tilde{a}_{i,j}^k=a_{i,j}^k-u_k$ for $k=w,s$; $\tilde{a}_{i,j}^k=a_{i,j}^k+u_k$ for $k=e,n$; u_k is the pore-scale flow velocity on the edge k; and $a_{i,j}^k(k=w,s,e,n)$ correspond to the coefficients a_k ($k=W$, S, E, N) in *Versteeg and Malalasekera* [2007, section 5.7]. The pore-scale finite-volume representation also contributes components to the right-hand side of global system (19),

$$b(l_{i,j})=\Delta_x\Delta_y c_{i,j}^n-(1-\theta)\Delta_t\Delta_y[q_{i,j}^n(w)+q_{i,j}^n(e)]-(1-\theta)\Delta_t\Delta_x[q_{i,j}^n(s)+q_{i,j}^n(n)], \tag{A4}$$

where $q_{i,j}^n(k)$ is the discretized mass flux (10) at time $t_n=n\Delta_t$.

[67] The global system's components (A1)–(A4) are modified for the interfacial volumes $v_{i,j}$ by incorporating the interfacial flux (14). Let $l_{(i,j)\text{-}k}^k$ denote the index of component $c(l_{(i,j)\text{-}k}^k)$ of vector **c** that represents pore-scale concentration $c_{(i,j)\text{-}k}^{n+1}$ at the edge (i,j)-k of the volume $v_{i,j}$ adjacent to interface Γ. For $k=w$, equations (A1) and (A2) are replaced with

$$A(l_{i,j},l_{i,j})=\Delta_x\Delta_y+\theta\Delta_t\Delta_y(\tilde{b}_{i,j}^w+\tilde{a}_{i,j}^e)+\theta\Delta_t\Delta_x(\tilde{a}_{i,j}^s+\tilde{a}_{i,j}^n) \tag{A5}$$

and

$$A(l_{i,j},l_{(i,j)\text{-}w}^w)=-\theta\Delta_t\Delta_y b_{i,j}^w. \tag{A6}$$

[68] For $k=e$, equations (A1) and (A2) are replaced with

$$A(l_{i,j},l_{i,j})=\Delta_x\Delta_y+\theta\Delta_t\Delta_y(\tilde{a}_{i,j}^w+\tilde{b}_{i,j}^e)+\theta\Delta_t\Delta_x(\tilde{a}_{i,j}^s+\tilde{a}_{i,j}^n) \tag{A7}$$

and

$$A(l_{i,j},l_{(i,j)\text{-}e}^e)=-\theta\Delta_t\Delta_y b_{i,j}^e. \tag{A8}$$

[69] In equations (A5)–(A8), $\tilde{b}_{i,j}^k=b_{i,j}^k-u_k$ for $k=w$ and $\tilde{b}_{i,j}^k=b_{i,j}^k+u_k$ for $k=e$, where $b_{i,j}^k$ are the coefficients a_k in *Versteeg and Malalasekera* [2007, section 5.7] modified to account for the Dirichlet boundary condition at the edge k. This is done by discretizing the mass flux at the edge k between the edge k and the center of the volume $v_{i,j}$, instead of discretizing between the centers of the volumes v_{i_k,j_k} and $v_{i,j}$.

[70] Let l_I denote the index of component $c(l_I)$ of vector **c** that represents Darcy-scale concentration $\overline{c}_I^{N+1}$ at the center of volume V_I at time $t_{N+1}=(N+1)\Delta_T$. Let l_I^K denote the index of component $c(l_I^K)$ of vector **c** that represents Darcy-scale concentration $\overline{c}_{I_K}^{N+1}$ at the center of volume V_{I_K}, which shares the edge K ($K=W$ or E) with volume V_I. For reaction rate $R(\overline{c})=\tilde{K}(\overline{c}-c_{\text{eq}})$ with a Darcy-scale reaction rate constant $\tilde{K}$, finite-volume discretization (11) with control volumes V_I contributes the following components to the global finite-volume matrix **A** in equation (19)

$$A(l_I,l_I)=\Delta X\omega_I^{N+1}+\theta\Delta_T(\tilde{A}_I^W+\tilde{A}_I^E+\Delta X\tilde{K}_I^{N+1}) \tag{A9}$$

and

$$A(l_I,l_I^K)=-\theta\Delta_T A_I^K, \qquad K=W,E \tag{A10}$$

where $\tilde{A}_I^W=A_I^W-U_W$, $\tilde{A}_I^E=A_I^E+U_E$, and U_K is the Darcy-scale flow velocity on the edge K ($K=W,E$). The Darcy-scale finite-volume representation also contributes components to the right-hand side of global system (19),

$$b(l_I)=\Delta X\omega_I^N\overline{c}_I^N+\Delta X\Delta_T[\theta\tilde{K}_I^{N+1}+(1-\theta)\tilde{K}_I^N]c_{\text{eq}}-(1-\theta)\Delta_T[\overline{q}_I^N(W)+\overline{q}_I^N(E)+\Delta X\tilde{K}_I^N\overline{c}_I^N] \tag{A11}$$

where $\overline{q}_I^N(K)$ is the discretized mass flux (13) at time $t_N=N\Delta_T$, and $\tilde{K}_I^N$ is the Darcy-scale reaction rate constant in volume V_I at time t_N.

[71] The global system's components (A9)–(A11) are modified for the interfacial volumes V_I by incorporating the interfacial flux (15). Let $l_{I\text{-}K}^K$ denote the index of component $c(l_{I\text{-}K}^K)$ of vector **c** that represents Darcy-scale concentration $c_{I\text{-}K}^{N+1}$ at the edge $(I\text{-}K)$ of the volume V_I adjacent to interface. For $K=W$, equations (A9) and (A10) are replaced with

$$A(l_I,l_I)=\Delta X\omega_I^{N+1}+\theta\Delta_T(\tilde{B}_I^W+\tilde{A}_I^E) \tag{A12}$$

and

$$A(l_I,l_{I\text{-}W}^W)=-\theta\Delta_T B_I^W. \tag{A13}$$

[72] For $K=E$, equations (A9) and (A10) are replaced with

$$A(l_I, l_I) = \Delta X \omega_I^{N+1} + \theta \Delta_T (\tilde{A}_I^W + \tilde{B}_I^E) \tag{A14}$$

and

$$A(l_I, l_{I\text{-}E}^E) = -\theta \Delta_T B_I^E \tag{A15}$$

[73] In equations (A12)–(A15), $\tilde{B}_I^K = B_I^K - U_K$ for $K = W$ and $\tilde{B}_I^K = B_I^K + U_K$ for $K = E$, where B_I^K are the modified coefficients B_I^K that account for the Dirichlet boundary condition at the edge K. This is done by discretizing the mass flux at the edge K between the edge K and the center of the volume V_I instead of between the centers of the volumes V_{I_K} and V_I.

[74] The FCC implementation of the continuity conditions along the pore-scale/Darcy-scale interface Γ combines the first of equations (16) and the second of equations (17). The former is expressed as

$$A(l_{I\text{-}K}^K, l_{I\text{-}K}^K) = 1 \qquad A(l_{I\text{-}K}^K, l_{(i',j)\text{-}k}^k) = -\frac{\Delta_y}{H_I^K}. \tag{A16}$$

The latter takes the form

$$A(l_{(i',j)\text{-}k}^k, l_{(i',j)\text{-}k}^k) = b_{i',j}^k \tag{A17}$$

$$A(l_{(i',j)\text{-}k}^k, l_{I',j}) = \tilde{b}_{i',j}^k \tag{A18}$$

$$A(l_{(i',j)\text{-}k}^k, l_{I\text{-}K}^K) = \beta_{i',j} B_I^K \tag{A19}$$

$$A(l_{(i',j)\text{-}k}^k, l_I) = \beta_{i',j} \tilde{B}_I^K. \tag{A20}$$

[75] The alternative FFC implementation of the continuity conditions along the pore-scale/Darcy-scale interface Γ combines the second of equations (16) and the first of equations (17). It replaces equations (A16)–(A20) with

$$A(l_{I\text{-}K}^K, l_{I\text{-}K}^K) = B_I^K \qquad A(l_{I\text{-}K}^K, l_I) = \tilde{B}_I^K \tag{A21}$$

and

$$A(l_{I\text{-}K}^K, l_{(i',j)\text{-}k}^k) = \frac{\Delta_y}{H_I^K} b_{i',j}^k \tag{A22}$$

$$A(l_{I\text{-}K}^K, l_{I',j}) = \frac{\Delta_y}{H_I^K} \tilde{b}_{i',j}^k \tag{A23}$$

$$A(l_{(i',j)\text{-}k}^k, l_{(i',j)\text{-}k}^k) = 1 \tag{A24}$$

$$A(l_{(i',j)\text{-}k}^k, l_{I\text{-}K}^K) = -\alpha_{i',j}. \tag{A25}$$

Appendix B: Cellular Automaton

[76] We use a cellular automaton algorithm (CAA) to model surface growth at the pore scale. The pore space is discretized with a regular mesh. CAA assigns each element of the mesh one of the two binary states: *Solid Element* (SE) or *Active Element* (AE). The SE state is assigned to all elements representing the solid matrix (e.g., fracture walls or solid grains of a porous material). The AE state is assigned to all other elements representing the pore space occupied by fluid. An AE that shares at least one edge with a SE is referred to as a *Growing Element* (GE). Such an edge is called a *Reactive Edge* (RE). Each RE is characterized by its position in the associated AE and is assigned a value of the reaction rate constant. The RE's position changes when the fluid/solid interface invades the corresponding AE; its initial value is set to 0.

[77] Simulation time $t_n^g = n\Delta_t^g (n = 0, \ldots, n_t - 1)$ is discretized into n_t time steps Δ_t^g. Flow velocity and solute concentration are evaluated in all AEs. Given the elements' positions and states at time t_n^g, the following algorithm is used to advance the system to time t_{n+1}^g.

[78] 1. Determine REs k_{i_m,j_m} in each GE (i_m, j_m):

[79] i. Use equation (4) to find the position of the fluid/solid interface, $x_{k_{i_m,j_m}}^{n+1}$, of RE k_{i_m,j_m} at t_{n+1}^g

$$x_{k_{i_m,j_m}}^{n+1} = x_{k_{i_m,j_m}}^n + \frac{r_s(c_{i_m,j_m}^n)}{\rho_s} \Delta_t^g \tag{B1}$$

where c_{i_m,j_m}^n is the concentration in GE (i_m, j_m) at t_n^g

[80] ii. Compute the solid surface advancing into GE (i_m, j_m)

$$s_{k_{i_m,j_m}}^{n+1} = x_{k_{i_m,j_m}}^{n+1} \Delta_{k_{i_m,j_m}} \tag{B2}$$

where $\Delta_{k_{i_m,j_m}}$ is the length of RE k_{i_m,j_m} defined by

$$\Delta_{k_{i_m,j_m}} = \begin{cases} \Delta_y & \text{if RE } k_{i_m,j_m} \text{ is west/east edge} \\ \Delta_x & \text{if RE } k_{i_m,j_m} \text{ is south/north edge} \end{cases}$$

[81] iii. Compute the solid surface in GE (i_m, j_m),

$$S_{i_m,j_m}^{n+1} = \sum_{k_{i_m,j_m}=1}^{N_{i_m,j_m}} s_{k_{i_m,j_m}}^{n+1}, \tag{B3}$$

where N_{i_m,j_m} is the number of REs in GE (i_m, j_m)

[82] 2. Compare S_{i_m,j_m}^{n+1} and the element's area

[83] If $S_{i_m,j_m}^{n+1} < \Delta_x \Delta_y$ then
store $x_{k_{i_m,j_m}}^{n+1}$ for each RE for next iteration

[84] If $S_{i_m,j_m}^{n+1} \geq \Delta_x \Delta_y$ then
relabel this GE as SE;
update the list of GEs by identifying AEs surrounding the new SE;
identify REs of the new GEs;
redistribute $S_{i_m,j_m}^{n+1} - \Delta_x \Delta_y$ between these REs.

[85] **Acknowledgments.** This research was supported in part by the National Science Foundation award EAR-1246315 and by the Computational Mathematics Program of the Air Force Office of Scientific Research.

References

Balhoff, M. T., S. G. Thomas, and M. F. Wheeler (2008), Mortar coupling and upscaling of pore-scale models, *Comput. Geosci.*, *12*(1), 15–27, doi: 10.1007/s10596-007-9058-6.

Battiato, I., and D. M. Tartakovsky (2011), Applicability regimes for macroscopic models of reactive transport in porous media, *J. Contam. Hydrol.*, *120–121*, 18–26.

Battiato, I., D. M. Tartakovsky, A. M. Tartakovsky, and T. Scheibe (2009), On breakdown of macroscopic models of mixing-controlled heterogeneous reactions in porous media, *Adv. Water Resour.*, *32*, 1664–1673, doi: 10.1016/j.advwatres.2009.08.008.

Battiato, I., D. M. Tartakovsky, A. M. Tartakovsky, and T. D. Scheibe (2011), Hybrid models of reactive transport in porous and fractured media, *Adv. Water Resour.*, *34*(9), 1140–1150.

Berkowitz, B., and J. Y. Zhou (1996), Reactive solute transport in a single fracture, *Water Resour. Res.*, *32*(4), 901–913.

Boso, F., and I. Battiato (2013), Homogenizability conditions for multicomponent reactive transport, *Adv. Water Resour.*, doi:10.1016/j.advwatres.2013.07.014.

Davis, T. A. (2004), Algorithm 832: UMFPACK v4.3—An unsymmetric-pattern multifrontal method, *ACM Trans. Math. Software*, *30*(2), 196–199, doi:10.1145/992200.992206.

Dijk, P., and B. Berkowitz (1998), Precipitation and dissolution of reactive solutes in fractures, *Water Resour. Res.*, *34*(3), 457–470, doi:10.1029/97WR03238.

Gerya, T. (2010), *Introduction to Numerical Geodynamic Modeling*, Cambridge Univ. Press, Cambridge, U. K.

Ivanov, V., and J. Chu (2008), Applications of microorganisms to geotechnical engineering for bioclogging and biocementation of soil in situ, *Rev. Environ. Sci. Biotechnol.*, *7*(2), 139–153.

Leemput, P. V., C. Vandekerckhove, W. Vanroose, and D. Roose (2007), Accuracy of hybrid lattice Boltzmann/finite difference schemes for reaction-diffusion systems, *Multiscale Model. Simul.*, *6*(3), 838–857.

Mehmani, Y., T. Sun, M. T. Balhoff, P. Eichhubl, and S. Bryant (2012), Multiblock pore-scale modeling and upscaling of reactive transport: Application to carbon sequestration, *Transp. Porous Media*, *95*(2), 305–326, doi:10.1007/s11242-012-0044-7.

Mikelic, A., V. Devigne, and C. J. V. Duijn (2006), Rigorous upscaling of the reactive flow through a pore, under dominant Peclet and Damkohler numbers, *SIAM J. Math. Anal.*, *38*(4), 1262–1287.

Noiriel, C., B. Made, and P. Gouze (2007), Impact of coating development on the hydraulic and transport properties in argillaceous limestone fracture, *Water Resour. Res.*, *43*, W09406, doi:10.1029/2006WR005379.

Park, S.-W., M. Intaglietta, and D. M. Tartakovsky (2012), Impact of endothelium roughness on blood flow, *J. Theor. Biol.*, *300*, 152–160, doi:10.1016/j.jtbi.2012.01.017.

Roubinet, D., J.-R. de Dreuzy, and P. Davy (2010a), Connectivity-consistent mapping method for 2-D discrete fracture networks, *Water Resour. Res.*, *46*, W07532, doi:10.1029/2009WR008302.

Roubinet, D., H.-H. Liu, and J.-R. de Dreuzy (2010b), A new particle-tracking approach to simulating transport in heterogeneous fractured porous media, *Water Resour. Res.*, *46*, W11507, doi:10.1029/2010WR009371.

Roubinet, D., J.-R. de Dreuzy, and D. M. Tartakovsky (2012), Semi-analytical solutions for solute transport and exchange in fractured porous media, *Water Resour. Res.*, *48*, W01542, doi:10.1029/2011WR011168.

Tartakovsky, A. M., P. Meakin, T. D. Scheibe, and B. D. Wood (2007), A smoothed particle hydrodynamics model for reactive transport and mineral precipitation in porous and fractured porous media, *Water Resour. Res.*, *43*, W05437, doi:10.1029/2005WR004770.

Tartakovsky, A. M., G. Redden, P. C. Lichtner, T. D. Scheibe, and P. Meakin (2008a), Mixing-induced precipitation: Experimental study and multiscale numerical analysis, *Water Resour. Res.*, *44*, W06S04, doi:10.1029/2006WR005725.

Tartakovsky, A. M., D. M. Tartakovsky, T. D. Scheibe, and P. Meakin (2008b), Hybrid simulations of reaction-diffusion systems in porous media, *SIAM J. Sci. Comput.*, *30*(6), 2799–2816.

Tartakovsky, D. M., and D. Xiu (2006), Stochastic analysis of transport in tubes with rough walls, *J. Comput. Phys.*, *217*(1), 248–259.

Tomin, P., and I. Lunati (2013), Hybrid multiscale finite volume method for two-phase flow in porous media, *J. Comput. Phys.*, *250*, 293–307, doi:10.1016/j.jcp.2013.05.019.

Versteeg, H., and M. Malalasekera (2007), *An Introduction to Computational Fluid Dynamics: The Finite Volume Method*, Pearson, Harlow, U. K.

Zayernouri, M., S.-W. Park, D. M. Tartakovsky, and G. E. Karniadakis (2013), Stochastic smoothed profile method for modeling random roughness in flow problems, *Comput. Methods Appl. Mech. Eng.*, *263*, 99–112, doi:10.1016/j.cma.2013.05.007.